Dalton Transactions

COMMUNICATION

View Article Online
View Journal | View Issue

Open Access Article. Published on 17 November 2015. Downloaded on 4/2/2026 3:35:01 PM.
This article is licensed under a Creative Commons Attribution 3.0 Unported Licence.

Cite this: *Dalton Trans.*, 2016, **45**, 78

Received 1st August 2015,
Accepted 16th November 2015

DOI: 10.1039/c5dt02974k

www.rsc.org/dalton

Enhanced visible and near infrared emissions *via* Ce^{3+} to Ln^{3+} energy transfer in Ln^{3+}-doped CeF_3 nanocrystals (Ln = Nd and Sm)†

Tuhin Samanta, Shyam Sarkar, Venkata. N. K. B. Adusumalli, Athma E. Praveen and Venkataramanan Mahalingam*

We report the enhancement of both visible and near infrared (NIR) emissions from Nd^{3+} ions *via* Ce^{3+} sensitization in colloidal nanocrystals for the first time. This is achieved in citrate capped Nd^{3+}-doped CeF_3 nanocrystals under ultraviolet (UV) irradiation (λ_{ex} = 282 nm). The lasing transition ($^4F_{3/2} \rightarrow {}^4I_{11/2}$) at 1064 nm from Nd^{3+}-doped CeF_3 nanocrystals has much higher emission intensity *via* Ce^{3+} ion sensitization compared to the direct excitation of Nd^{3+} ions. The nanocrystals were prepared using a simple microwave irradiation route. Moreover, the study has been extended to Sm^{3+}-doped CeF_3 nanocrystals which show strong characteristic emissions of Sm^{3+} ions *via* energy transfer from Ce^{3+} ions. The energy transfer mechanism from Ce^{3+} to Nd^{3+} and Sm^{3+} ions is proposed.

1. Introduction

There is a surge in research interest towards developing lanthanide (Ln^{3+})-doped nanomaterials as they show sharp luminescence signals with longer excited state lifetimes (in the range of μs to ms). In addition, Ln^{3+} ions show luminescence peaks over a wide electromagnetic spectrum. Particularly interesting are those emitting in the near-infrared (NIR) region *i.e.* the spectrum with the wavelength range of 700 to 2100 nm. NIR luminescence of lanthanide ions (Ln^{3+}) finds applications in NIR LED technology, lasers, solar energy conversion, medical science and telecommunication.[1–4] For example, Ln^{3+} ions such as Er^{3+}, Nd^{3+}, Tm^{3+} and Ho^{3+} have characteristic emissions in the NIR region and can be used as active materials for developing optical amplifiers.[5–7] In addition, NIR emission is quite valuable for biological applications because of lower scattering from the body than visible photons, low auto-fluorescence, deep penetration and being transparent to biological tissues.[8–11] However, Ln^{3+} ions in aqueous media show very weak emission intensities owing to their low molar absorption coefficients (2–10 M^{-1} cm^{-1}), which is attributed to both spin- and parity-forbidden 4f–4f transitions of Ln^{3+} ions.[12–14] In addition, nonradiative transitions are very efficient in aqueous medium leading to further reduction of luminescence efficiency. One way to improve the luminescence efficiency is *via* an antenna effect, where typically an organic fluorophore possessing a high absorption coefficient is used as a sensitizer for Ln^{3+} ions. The organic fluorophore transfers the absorbed energy to Ln^{3+} ions leading to an enhanced luminescence quantum efficiency of Ln^{3+} ions. However, most of the reports on the antenna effect are restricted to Ln^{3+} complexes.[15,16] Moreover, organic molecules generally photobleach and are relatively less stable. On the other hand, Ce^{3+} ions can be used as a sensitizer as they possess a high absorbance coefficient (~10^{-18} cm^2) due to allowed 4f–5d transitions.[17–20] The optical characteristics of Ce^{3+} ions for efficient energy transfer are mainly attributed to two reasons: broad emission leading to better overlapping with absorption bands of other Ln^{3+} ions and faster luminescence decay.[21–24] However, sensitization of luminescence *via* Ce^{3+} ions is mostly restricted to visible emission of Tb^{3+} ions and to some extent Dy^{3+} ions.[25,26] Recently, we have used Ce^{3+} ions for sensitizing Tm^{3+} ions to obtain single band blue emission from $NaYF_4$ nanocrystals.[27]

Our objective is to sensitize NIR emissions using Ce^{3+} ions. Among NIR emitting Ln^{3+} ions, Nd^{3+} and Sm^{3+} are interesting for the following reasons. For example, Nd^{3+} ions show an important laser transition at 1064 nm (*e.g.* Nd^{3+}-doped $Y_3Al_5O_{12}$).[28–30] In fact the 1064 nm is used for achieving 532 nm *via* second harmonic generation. Furthermore, this emission due to the transition from $^4F_{3/2} \rightarrow {}^4I_{11/2}$ energy levels falls well in the second "human optical window" (1000–1350 nm).[31–35] Similarly, Sm^{3+} ions show two emissions in this optical window (near 1020 and 1150 nm) in addition to a strong emission at 940 nm. Moreover, the emission of Nd^{3+} shows remarkable thermal sensitivity leading to their use as

Department of Chemical Sciences, Indian Institute of Science Education and Research (IISER), Kolkata, Mohanpur, West Bengal 741252, India.
E-mail: mvenkataramanan@yahoo.com; Fax: +91-33-25873020; Tel: +91(0)9007603474

†Electronic supplementary information (ESI) available: SEM, EDAX, TGA, PL spectra and digital images of water dispersion of Nd^{3+} doped CeF_3 nanocrystals. Lifetimes, XRD and energy transfer mechanism of Ce^{3+} to Sm^{3+} of Sm^{3+} doped CeF_3 nanocrystals. See DOI: 10.1039/c5dt02974k

This journal is © The Royal Society of Chemistry 2016

Open Access Article. Published on 17 November 2015. Downloaded on 4/2/2026 3:35:01 PM.
This article is licensed under a Creative Commons Attribution 3.0 Unported Licence.

sub-tissue thermal sensors.[36–38] However, both Nd^{3+} ions and Sm^{3+} ions show sharp f–f absorption which are difficult to pump.[39–41] Although there are quite a few reports on Ce^{3+} to Nd^{3+} energy transfer, they are mostly restricted to a glass matrix.[42–46] In fact, to our knowledge there are no reports on Ce^{3+} sensitized NIR emissions from Nd^{3+} or Sm^{3+} ions in colloidal nanocrystals, particularly in aqueous milieu.[47,48] This is important as there is increasing demand for NIR emitting materials for biological imaging applications. Furthermore, colloidal nanocrystals can easily be coated or incorporated in sol–gel systems which is helpful for thin film device fabrication.

In this article, we report enhanced visible and NIR luminescence from Nd^{3+}-doped CeF_3 nanocrystals *via* Ce^{3+} sensitization. The lasing transition ($^4F_{3/2} \rightarrow {}^4I_{11/2}$) at 1064 nm from Nd^{3+}-doped CeF_3 nanocrystals has shown emission strength about 3 times higher compared to that of the direct excitation of Nd^{3+} ions. Similarly, strong emissions in the NIR region are observed for Sm^{3+}-doped CeF_3 nanocrystals. We emphasize that all these are achieved from water and DMSO dispersible colloidal nanocrystals which can be useful for bioimaging applications.

2. Experimental section

2.1. Materials

Cerium nitrate [$Ce(NO_3)_3$, 99.98%], neodymium oxide [Nd_2O_3, 99.9%], samarium nitrate [$Sm(NO_3)_3$, 99.9%], trisodium citrate (>98%), sodium tetrafluoroborate (98%) and absolute ethanol were purchased from Sigma Aldrich. All chemicals were of analytical grade and used without further purification. Double distilled water was used throughout the synthesis and characterization.

2.2. Synthesis

Citrate functionalized Ln^{3+}-doped CeF_3 nanocrystals were prepared by a simple microwave assisted method. Briefly, 0.95 mmol of $Ce(NO_3)_3$ and 0.05 mmol of $Nd(NO_3)_3$ were taken in a 100 ml round bottom flask and completely dissolved in 15 ml of double distilled water. To this clear aqueous solution 1.5 mmol $NaBF_4$ and 4 mmol trisodium citrate (TSC) were added and stirred until complete dissolution. The mixture was magnetically stirred for 15 minutes at room temperature. Finally the mixture was transferred to a 30 ml vial, used for microwave synthesis. The synthesis was carried out using the Anton Parr 300 microwave reactor. The vial was tightly sealed with a Teflon cap and the reaction was carried out at 180 °C for 10 minutes and then cooled to room temperature. The product was collected by centrifugation and washed thrice with absolute ethanol. It should be noted that the microwave experiments were carried out in temperature control mode. Simultaneous gas jet cooling (3–5 bar) during microwave irradiation was performed by using compressed air (6 bar). All microwave experiments were carried out using magnetic stirring at a rate of 600 rpm. The same protocol was used for the synthesis of citrate capped Sm^{3+}-doped CeF_3 nanocrystals. [0.97 mmol of $Ce(NO_3)_3$ and 0.03 mmol of $Sm(NO_3)_3$ in 15 mL double distilled water.]

2.3. Characterization

Powder X-ray diffraction (PXRD) measurements were performed on a Rigaku-smartlab diffractometer with Cu Kα operating at 70 kV and 35 mA at a scanning rate of 1° min^{-1} in the 2θ range from 20° to 80°. The samples were completely powdered and spread evenly on a quartz slide. TEM measurement was carried out using a high resolution FEG transmission electron microscope (JEOL, JEM 2100F) with a 200 keV electron source. Briefly, a drop of the CeF_3 nanocrystals in water was taken on a strong carbon coated 300 mesh Cu grid and dried in air. The FT-IR spectra were obtained with a Perkin Elmer Spectrum RX1 spectrophotometer with the KBr disk technique in the range of 400–4000 cm^{-1}. Thermogravimetric analysis was performed using the Mettler Toledo TGA 851 instrument under a N_2 atmosphere at a heating rate of 10° min^{-1}. The photoluminescence measurements were performed with the Horiba Jobin Yvon Fluorolog. All the emission spectra were recorded using the steady state 450 W Xe lamp as the excitation source. The luminescence lifetime measurements were performed using the Horiba Jobin Yvon Fluorolog machine with a pulsed Xe source of 150 W.

3. Results and discussion

3.1. Phase and structure

The phase analysis of the Ln^{3+}-doped CeF_3 (Ln = Nd and Sm) nanocrystals was performed using powder X-ray diffraction (XRD) measurements. Fig. 1 shows the XRD pattern of the Nd^{3+}-doped CeF_3 nanocrystals along with that of a standard pattern for bulk CeF_3. All the peaks are matched well with that of the standard CeF_3 (ICSD PDF Card no. 00-038-0452) suggesting the formation of a pure hexagonal phase. The

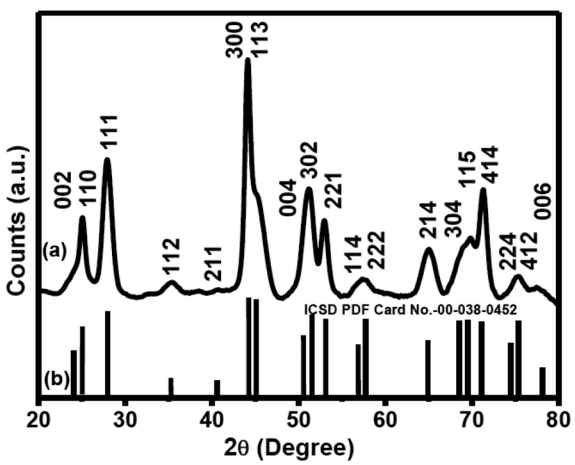

Fig. 1 Powder XRD patterns of (a) Nd^{3+}-doped CeF_3 nanocrystals and (b) standard hexagonal CeF_3 crystals (ICSD PDF Card No-00-038-0452).

Open Access Article. Published on 17 November 2015. Downloaded on 4/2/2026 3:35:01 PM.
This article is licensed under a Creative Commons Attribution 3.0 Unported Licence.

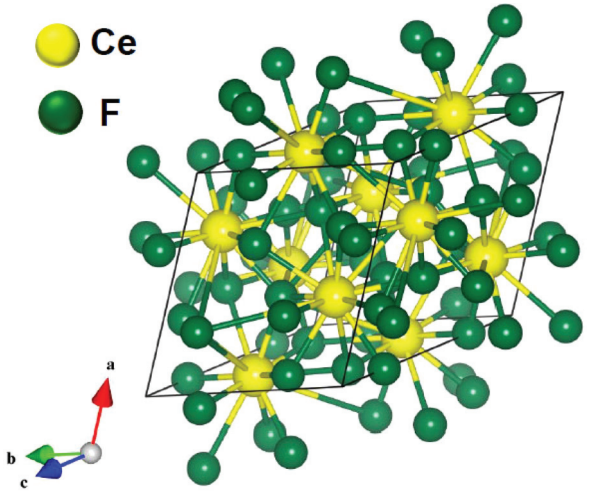

Fig. 2 Schematic presentation of the unit cell structure of CeF_3 nanocrystals.

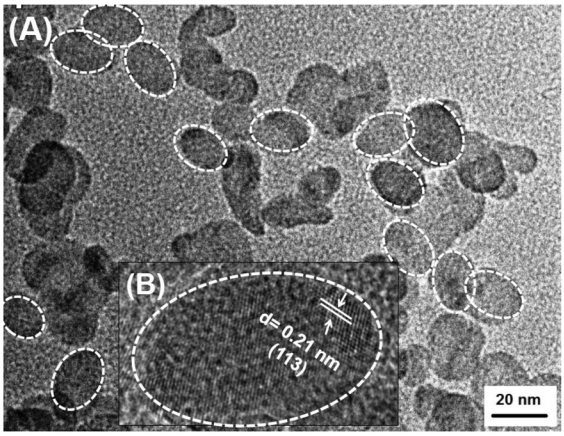

Fig. 3 TEM image of Nd^{3+}-doped CeF_3 nanocrystals and the inset shows the HR image of a nanocrystal. White color circles indicate the boundary of the nanocrystals.

miller indices for each peak are shown above the corresponding peaks.

The average crystallite size is found to be 8.5 nm as calculated using the Debye–Scherrer equation, $t = (0.9\lambda/\beta\cos\theta)$, where t stands for average crystallite size, λ denotes the wavelength (λ = 1.5418 Å) of incident X-ray, β denotes the corrected full width at half maximum (FWHM) and θ denotes the diffraction angle. Lattice parameters of Nd^{3+}-doped CeF_3 nanocrystals from XRD are found to be $a = b = 7.1024$, $c = 7.2612$ and $\alpha = \beta = 90°$, $\gamma = 120°$. The hexagonal phase CeF_3 nanocrystals adopt the same structure as LaF_3, and the space group of these two crystals is $P3c1$. The highest point group of this structure is D_{3d}. In this structure, the anion ligand number is 12, *i.e.* each cation is surrounded by 12 anions. The cation sits at the center of an icosahedron. Twelve fluorides are close: four at the bottom corners of the icosahedron, four in the faces of the icosahedron, and four at the top corners of the icosahedron. The cation can be considered as 12 coordinate. The schematic of the unit cell crystal structure of hexagonal CeF_3 obtained using the visualization for electronic and structural analysis (VESTA) program is shown in Fig. 2. The atomic coordinates (x, y and z) used for the calculations are used from the reported literature[49] and shown in Table S1 (see the ESI†).

3.2. Morphology analysis

The morphology of the citrate-functionalized Nd^{3+}-doped CeF_3 nanocrystals is obtained by transmission electron microscopy (TEM) as shown in Fig. 3. From the TEM image the formation of oval shaped nanocrystals is clear. The average aspect ratio of the Nd^{3+}-doped CeF_3 nanocrystals is found to be approximately 0.8 (length = 20 nm and breadth = 16 nm). For the semi-quantitative analysis of the elements present in the Nd^{3+}-doped CeF_3 nanocrystals energy-dispersive X-ray (EDX) analysis was performed. The EDX analysis spectrum of Nd^{3+}-doped CeF_3 nanocrystals are shown in Fig. S1 (see the ESI†). It confirms the presence of Ce, F, and Nd in the sample.

3.3. Surface functionalization

The high dispersibility of the citrate functionalized CeF_3 nanocrystals in water suggests the binding of citrate ions to the surface of the nanocrystals which is supported by the FTIR analysis. The FTIR spectra of citrate capped CeF_3 nanocrystals along with pure trisodium citrate molecules are shown in Fig. 4. For the free TSC, major peaks are observed near 3453, 2985, 1600 and 1399 cm^{-1}. The strong and broad stretching vibration band centered at 3448 cm^{-1} is assigned to O–H in TSC and the peak at 2952 cm^{-1} is attributed to the methylene (CH_2) stretching vibrations of the alkyl chains of TSC. The band at 1600 cm^{-1} is assigned to the C=O asymmetric stretching vibration of the $–COO^-$ group, and the band at 1399 cm^{-1} is due to symmetric stretching vibrations of C–O in the $–COO^-$ group of the TSC.[50] In the case of citrate capped Nd^{3+} doped

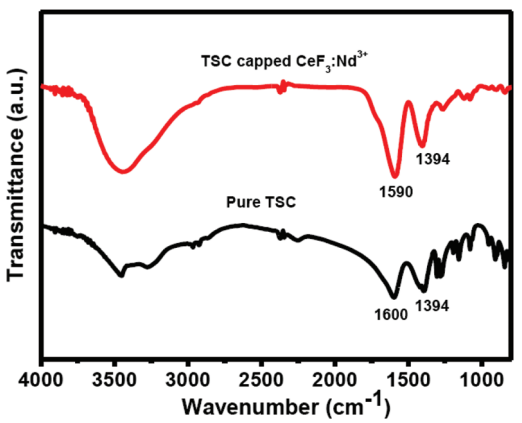

Fig. 4 FTIR spectra of citrate capped Nd^{3+}-doped CeF_3 nanocrystals and pure TSC molecules.

This journal is © The Royal Society of Chemistry 2016

Open Access Article. Published on 17 November 2015. Downloaded on 4/2/2026 3:35:01 PM.
This article is licensed under a Creative Commons Attribution 3.0 Unported Licence.

CeF_3 nanocrystals, all the characteristic peaks for TSC molecules are observed, however the C=O stretching frequency is shifted towards a lower wavenumber (at 1590 cm^{-1}) which clearly indicates the binding of the TSC ligand onto the surface of the Nd^{3+} doped CeF_3 nanocrystals.

To further confirm the citrate functionalization onto the surface of CeF_3 nanocrystals, TGA analysis was conducted. The TGA curves for both citrate capped CeF_3 nanocrystals and pure TSC are shown in Fig. S2, (see the ESI†). For the free TSC the major weight loss is noted from 250 °C due to the decomposition of TSC molecules. For the citrate functionalized CeF_3 nanocrystal, the onset of decomposition is shifted to the higher temperature (~275 °C) which further confirms that the citrate molecules are strongly attached to the surface of the CeF_3 nanocrystals. The wt% of citrate molecules attached to the CeF_3 is close to 3.12% as calculated from the weight loss from the TGA analysis. Further confirmation for the attachment of the citrate ligands to the nanocrystals comes from the high stability of the nanocrystals in water. The dispersion of the nanocrystals was relatively stable in water for more than 10 hours. The photoluminescence study suggests that the luminescence intensity of Nd^{3+} ions reduced by only ~30% after 10 hours. The digital images of the colloidal dispersion along with the corresponding emission spectra are shown in Fig. S3.†

3.4. Optical properties

Photoluminescence (PL) studies have been carried out for the colloidal 0.1 wt(%) Nd^{3+}-doped CeF_3 nanocrystals in water. Upon excitation at 282 nm, the nanocrystal dispersion shows visible and NIR emissions as shown in Fig. 5. The prominent band in the visible region is at 693 nm, which is assigned to the $^2I_{15/2} \rightarrow {}^4F_{7/2}$ transition. In addition, the nanocrystal dispersion shows characteristic NIR bands of Nd^{3+} ions at 1062 and 1339 nm in water, which are assigned to the $^4F_{3/2} \rightarrow {}^4I_{11/2}$ and $^4F_{3/2} \rightarrow {}^4I_{13/2}$ transitions, respectively. The most intense band at 1062 nm is potentially suitable for application in laser emission and telecommunication. The inset of Fig. 5 displays the excitation spectrum which shows an intense broad peak at 282 nm by monitoring the emission at 1062 nm. This peak is due to the 4f5d → 5f electronic transition of Ce^{3+} ions. This confirms the energy transfer from Ce^{3+} to Nd^{3+} ions. To further verify the occurrence of energy transfer, we prepared Nd^{3+}-doped (5 mol%) LaF_3 nanocrystals using the same synthesis protocol. Upon excitation at 280 nm, no characteristic emission from Nd^{3+} ions is observed confirming the energy transfer from Ce^{3+} to Nd^{3+} in Nd^{3+}-doped CeF_3 nanocrystals (see Fig. S4†). To understand the energy transfer efficiency, PL spectra of Nd^{3+}-doped CeF_3 nanocrystals were collected at direct excitation (514 nm) and 282 nm excitation. From Fig. 6, it is clear that upon 282 nm excitation the visible emission and NIR emission intensity increases by two and three times, respectively, compared to that of direct excitation. These results strongly suggest that efficient energy transfer occurs from Ce^{3+} to Nd^{3+} ions.

We have extended our study to check whether energy transfer from Ce^{3+} ions to Sm^{3+} ions is possible. The 3 mol(%) Sm^{3+}-doped CeF_3 nanocrystals were prepared using identical reaction conditions and characterized by XRD analysis. The XRD pattern suggests the formation of pure hexagonal phase CeF_3 nanocrystals as shown in Fig. S5.† The PL and excitation spectra of Sm^{3+} (3%)-doped CeF_3 nanocrystals are shown in Fig. 7. Upon 280 nm excitation the dispersion of Sm^{3+}-doped CeF_3 nanocrystals in DMSO shows intense peaks at 559, 593, 639 and 702 nm which are assigned to $^4G_{5/2} \rightarrow {}^6H_{5/2}$, $^4G_{5/2} \rightarrow {}^6H_{7/2}$, $^4G_{5/2} \rightarrow {}^6H_{9/2}$ and $^4G_{5/2} \rightarrow {}^6H_{11/2}$ transitions, respectively. The $^4G_{5/2} \rightarrow {}^6H_{5/2}$ transition at 560 nm has a magnetic dipole character.[51] The intensity ratio of $I(^4G_{5/2} \rightarrow {}^6H_{9/2})/I(^4G_{5/2} \rightarrow {}^6H_{5/2})$ is 1.05 which indicates lower polarizability of the chemi-

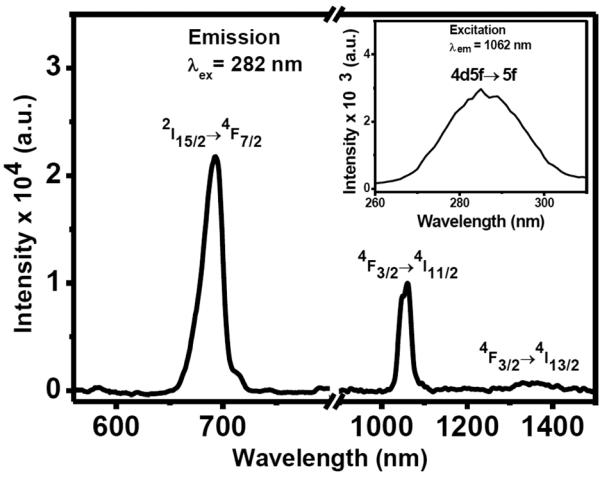

Fig. 5 PL spectrum of 5 mol(%) Nd^{3+}-doped CeF_3 nanocrystals in water covering the visible to NIR region (λ_{exi} = 282 nm). The inset shows the excitation spectrum for the same nanocrystals (λ_{emi} = 1062 nm).

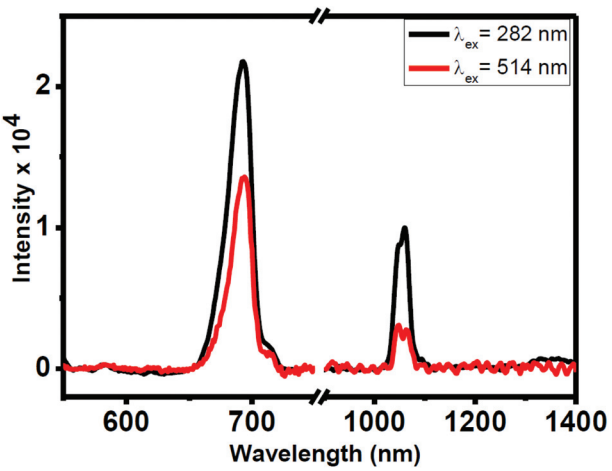

Fig. 6 PL spectra in the visible and NIR regions from Nd^{3+}-doped CeF_3 nanocrystals *via* Ce^{3+} ion excitation (282 nm) and direct excitation (512 nm).

Open Access Article. Published on 17 November 2015. Downloaded on 4/2/2026 3:35:01 PM.
This article is licensed under a Creative Commons Attribution 3.0 Unported Licence.

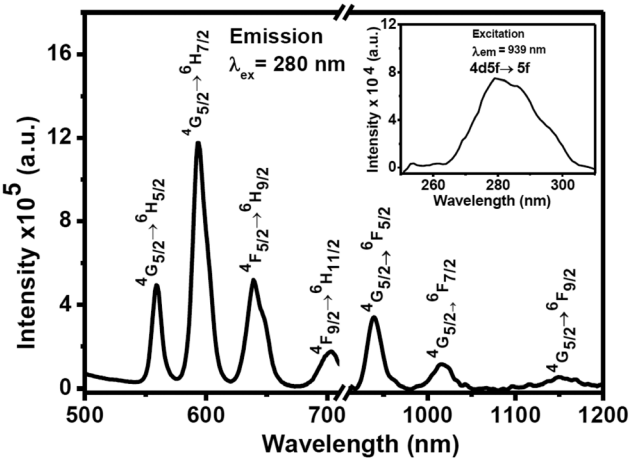

Fig. 7 PL spectrum of 3 mol(%) Sm^{3+}-doped CeF_3 nanocrystals in DMSO covering the visible to NIR region (λ_{ex} = 280 nm). The inset shows the excitation spectrum for the same nanocrystals (λ_{em} = 939 nm).

cal environment around the Sm^{3+} ions.[52] In addition, the nanocrystals show strong NIR emission peaks at 939 nm, 1017 nm and 1152 nm which are ascribed to the $^4G_{5/2} \rightarrow {}^6F_{5/2}$, $^4G_{5/2} \rightarrow {}^6F_{7/2}$, and $^4G_{5/2} \rightarrow {}^6F_{9/2}$ transitions, respectively. These transitions are characteristics of Sm^{3+} ions. Among these peaks, 939 peaks are quite intense and they fall in the first "human optical window". It is quite clear from Fig. S6,† that upon 280 nm excitation, both visible and NIR emission intensities increase by two times compared to that of direct excitation (400 nm). We have performed some control experiments to test the effect of the concentrations of Nd^{3+} and Ce^{3+} ions on the emission intensity of the nanocrystals. There is an increase in the emission intensity up to 5 mol% doping for the Nd^{3+} ions and there upon a decrease is noted. Similarly, the optimum doping concentration for Sm^{3+}-doped CeF_3 is found to be 3 mol% (see Fig. S7†).

Enhancement of visible and NIR emissions for both Nd^{3+} and Sm^{3+} ions is achieved *via* energy transfer from Ce^{3+} ions. This is supported by the overlap between the emission spectrum of Ce^{3+} ions with the absorbance of Sm^{3+} and Nd^{3+} ions. The results are shown in Fig. S8.† The energy transfer efficiency between the donor (Ce^{3+}) and acceptor (Nd^{3+}/Sm^{3+}) is evaluated using the equation $\eta = 1 - \tau_d/\tau_{d0}$. The average terms τ_d and τ_{d0} are denoted for the excited state lifetimes of the sensitizer in the presence and absence of the activator, respectively. The lifetimes of the sensitizer Ce^{3+} ions in the presence and absence of an emitter (*i.e.* Nd^{3+}/Sm^{3+} ions) are calculated using Time Correlated Single Photon Counting (TCSPC). The lifetime values of Ce^{3+} ions in CeF_3, CeF_3:Nd^{3+} (5%) and CeF_3:Sm^{3+} (3%) nanocrystals are found to be 23 ns, 9.7 ns and 12 ns, respectively.[53] Lifetime decay curves are shown in Fig. S9 (see the ESI†). The calculated energy transfer efficiencies from Ce^{3+} to Nd^{3+} and Sm^{3+} are close to 57% and 48%, respectively. To understand the effect of Nd^{3+} concentration in CeF_3 on the energy transfer efficiency between Ce^{3+} and Nd^{3+}, we have calculated the corresponding lifetimes of Ce^{3+} emissions. It is interesting to note that the energy transfer efficiency increases with the increase in the Nd concentration. The values are 53%, 55%, 57% and ~80% respectively, for 1, 3, 5 and 8 mol% Nd^{3+} doping in CeF_3 nanocrystals. Please note that the optimum luminescence efficiency of Nd^{3+} is 5 mol%. This suggests that though there is a higher energy transfer probability between Ce^{3+} to Nd^{3+} at a higher doping concentration, the cross relaxation between Nd^{3+}–Nd^{3+} is higher leading to self-quenching of the luminescence. The lifetime decay curves are shown in Fig. S10.† Furthermore, we have measured the lifetimes of Sm^{3+} and Nd^{3+} ions in Sm^{3+} and Nd^{3+} doped CeF_3 nanocrystals, respectively. The lifetime of Sm^{3+} ions is 741 μs when excited at 282 nm and emission was monitored at 599 nm. The lifetime of Nd^{3+} ions is 8 μs when excited at 282 nm and emission was monitored at 693 nm as shown in Fig. S11.† [53]

3.5. Energy transfer mechanism

The proposed energy transfer mechanism between Ce^{3+} to Nd^{3+} ions and Sm^{3+} ions is schematically shown in Fig. 8. Upon 282 nm excitation, Ce^{3+} ions get excited from $4f^1$ to $4f^05d^1$ levels. A radiative energy transfer occurs from the relaxed lowest 4f5d energy level of Ce^{3+} ions to the $^2I_{15/2}$ energy level of Nd^{3+} ions followed by radiative transfer to the low lying $^4F_{7/2}$ level of Nd^{3+} ions. Subsequently, energy transfer from $^4F_{7/2}$ to $^4F_{3/2}$ occurs nonradiatively. Radiative relaxation from $^4F_{3/2}$ levels to the $^4I_{11/2}$ and $^4I_{13/2}$ energy levels of Nd^{3+} ions, lead to the 1064 nm and 1339 nm NIR emissions, respectively. Similarly, for Sm^{3+}-doped CeF_3 nanocrystals, upon 280 nm excitation, Ce^{3+} ions are excited from the $4f^05d^1 \rightarrow 4f^1$ level. A radiative energy transfer occurs from the lowest 4f5d energy band of Ce^{3+} ions to the $^4D_{1/2}$ energy level of Sm^{3+} ions followed by nonradiative transfer to the low lying $^4G_{5/2}$ level of Sm^{3+} ions. Subsequent decays from $^4G_{5/2}$ levels and $^6F_{9/2}$ levels to the $^6H_{5/2}$, $^6H_{7/2}$, $^6H_{9/2}$, $^6H_{11/2}$, $^6F_{5/2}$, $^6F_{7/2}$ and $^6F_{9/2}$ Sm^{3+} ions, result in emissions in the visible and NIR regions.

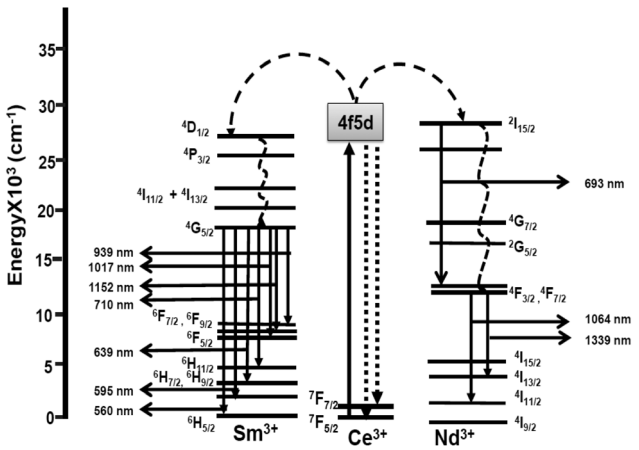

Fig. 8 Schematic of the proposed energy transfer mechanism from Ce^{3+} ions to Nd^{3+} and Sm^{3+} ions.

This journal is © The Royal Society of Chemistry 2016

Open Access Article. Published on 17 November 2015. Downloaded on 4/2/2026 3:35:01 PM.
This article is licensed under a Creative Commons Attribution 3.0 Unported Licence.

4. Conclusions

In conclusion, we have successfully synthesized hexagonal phase Ln^{3+} doped CeF_3 nanocrystals *via* a microwave assisted method. The morphology of the nanocrystals was oval shaped with an average aspect ratio of ~0.8. The nanocrystals are functionalized with citrate molecules which render them highly water dispersible. In Nd^{3+} and Sm^{3+}-doped CeF_3 nanocrystals, enhanced visible and near infrared (NIR) emissions were observed *via* Ce^{3+} ion sensitization upon ultraviolet (UV) irradiation (λ_{exi} = 280 nm). The energy transfer mechanism from Ce^{3+} to Nd^{3+} and Sm^{3+} ions is proposed. The strong NIR emissions from water dispersible nanocrystals are advantageous for bioimaging applications. In addition, they can easily be incorporated into polymers and other sol–gel matrices for the fabrication of devices for telecommunications.

Acknowledgements

VM thanks the Council of Scientific and Industrial Research (CSIR), Department of Science and Technology (DST), India and IISER-Kolkata for funding. TS, SS and VNKBA thank University Grand Commission (UGC), India for the scholarship.

Notes and references

1 S. Mishra, E. Jeanneau, A.-L. Bulin, G. Ledoux, B. Jouguet, D. Amans, A. Belsky, S. Danieleb and C. Dujardin, *Dalton Trans.*, 2013, **42**, 12633.
2 S. K. Singh, *RSC Adv.*, 2014, **4**, 58674.
3 M. Balestrieri, S. Colis, M. Gallart, G. Ferblantier, D. Muller, P. Gilliot, P. Bazylewski, G. S. Chang, A. Slaouib and A. Diniaa, *J. Mater. Chem. C*, 2014, **2**, 9182.
4 (*a*) P. Liu, J. Liu, X. Zheng, H. Luo, X. Li, Z. Yao, X. Yu, X. Shi, B. Hou and Y. Xia, *J. Mater. Chem. C*, 2014, **2**, 5769; (*b*) C. Hazra, T. Samanta, A. V. Asaithambi and V. Mahalingam, *Dalton Trans.*, 2014, **43**, 6623.
5 G. Gao, M. Peng and L. Wondraczek, *J. Mater. Chem. C*, 2014, **2**, 8083.
6 Z.-P. Zheng, X.-X. Zhang, T. Li, J. Yang, L.-M. Wei, L.-G. Zhang, X.-M. Lina and Y.-P. Cai, *Dalton Trans.*, 2014, **43**, 14009.
7 J. Zhang and S. Petoud, *Chem. – Eur. J.*, 2008, **14**, 1264.
8 D. Wang, B. Xue, X. Kong, L. Tu, X. Liu, Y. Zhang, Y. Chang, Y. Luo, H. Zhaoc and H. Zhang, *Nanoscale*, 2015, **7**, 190.
9 D. Tu, L. Liu, Q. Ju, Y. Liu, H. Zhu, R. Li and X. Chen, *Angew. Chem., Int. Ed.*, 2011, **50**, 6306.
10 E. Hemmer, N. Venkatachalam, H. Hyodo, A. Hattori, Y. Ebina, H. Kishimoto and K. Soga, *Nanoscale*, 2013, **5**, 11339.
11 (*a*) A. F. Collet, K. A. Gogick, K. A. White, S. Villette, A. Pallier, G. Collet, C. Kieda, T. Lib, S. J. Geib, N. L. Rosi and S. Petoud, *Proc. Natl. Acad. Sci. U. S. A.*, 2013, **113**, 17199; (*b*) M. Pedroni, F. Piccinelli, T. Passuello, M. Giarola, G. Mariotto, S. Polizzi, M. Bettinellia and A. Speghini, *Nanoscale*, 2011, **3**, 1456.
12 Y. Liu, D. Tu, H. Zhu, R. Li, W. Luo and X. Chen, *Adv. Mater.*, 2010, **22**, 3266.
13 L. Li, Y. Su and G. Li, *J. Mater. Chem.*, 2010, **20**, 459.
14 Z. Zhang, H. Feng, L. Liu, C. Yu, X. Lü, X. Zhu, W.-K. Wong, R. A. Jones, M. Pand and C. Su, *Dalton Trans.*, 2015, **44**, 6229.
15 J.-C. G. Bünzli and C. Piguet, *Chem. Soc. Rev.*, 2005, **34**, 1048.
16 (*a*) O. A. Blackburn, M. Tropiano, T. J. Sørensen, J. Thom, A. Beeby, L. M. Bushby, D. Parker, L. S. Natrajan and S. Faulkner, *Phys. Chem. Chem. Phys.*, 2012, **14**, 13378; (*b*) T. Samanta, C. Hazra and V. Mahalingam, *New J. Chem.*, 2015, **39**, 106.
17 S. Wu, C. Li, W. Wei, H. Wang, Y. Song, Y. Zhu and L. Lu, *J. Rare Earths*, 2010, **28**, 171.
18 Z. Fang, R. Cao, F. Zhang, Z. Ma, G. Donga and J. Qiu, *J. Mater. Chem. C*, 2014, **2**, 2204.
19 B. Gao, Q. Yan, Y. Tong, X. Zhang, H. Ma b, J.-l. Adam, J. Ren and G. Chen, *J. Lumin.*, 2013, **143**, 181.
20 D. Chen, Y. Wang, Y. Yu, P. Huang and F. Weng, *J. Appl. Phys.*, 2008, **104**, 116105.
21 M. C. Tan, G. A. Kumar and R. E. Riman, *Opt. Express*, 2009, **17**, 15904.
22 Y. V. Orlovskii, T. T. Basiev, E. O. Orlovskaya, Y. S. Privisa, V. V. Fedorov and S. B. Mirov, *J. Lumin.*, 2003, **101**, 211.
23 J. Mares, B. Jacquier, C. Pédrini and G. Boulon, *Rev. Phys. Appl.*, 1987, **22**, 145.
24 J. Ueda, P. Dorenbos, A. J. J. Bos, K. Kuroishia and S. Tanabea, *J. Mater. Chem. C*, 2015, **3**, 5642.
25 K. Li, M. Shang, D. Geng, H. Lian, Y. Zhang, J. Fan and J. Lin, *Inorg. Chem.*, 2014, **53**, 6743.
26 G. V. L. Reddy, L. R. Moorthy, T. Chengaiah and B. C. Jamalaiah, *Adv. Mater. Lett.*, 2013, **4**, 841.
27 V. N. K. B. Adusumalli, S. Sarkar and V. Mahalingam, *ChemPhysChem*, 2015, **16**, 2313.
28 L. Tong, J. Lou, Y. Xu, Q. Luo, N. Shen and E. Mazur, *Appl. Opt.*, 2002, **41**, 4008.
29 S. Satapathy, A. Ahlawat, A. Paliwal, R. Singh, M. K. Singh and P. K. Gupta, *CrystEngComm*, 2014, **16**, 2723.
30 P. Samuel, G. A. Kumar, T. Yanagitani, H. Yagi, K. I. Ueda and S. M. Babu, *Opt. Mater.*, 2011, **34**, 303.
31 A. M. Smith, M. C. Mancini and S. Nie, *Nat. Nanotechnol.*, 2009, **4**, 710.
32 (*a*) R. Wang and F. Zhang, *J. Mater. Chem. B*, 2014, **2**, 2422; (*b*) N. Bogdan, F. Vetrone, G. A. Ozin and J. A. Capobianco, *Nano Lett.*, 2011, **11**, 835.
33 N. Won, S. Jeong, K. Kim, J. Kwag, J. Park, S. G. Kim and S. Kim, *Mol. Imaging*, 2012, **11**, 338.
34 G. Hong, Y. Zou, A. L. Antaris, S. Diao, D. Wu, K. Cheng, X. Zhang, C. Chen, B. Liu, Y. He, J. Z. Wu, J. Yuan, B. Zhang, Z. Tao, C. Fukunaga and H. Dai, *Nat. Commun.*, 2014, **5**, 4206.

Open Access Article. Published on 17 November 2015. Downloaded on 4/2/2026 3:35:01 PM.
This article is licensed under a Creative Commons Attribution 3.0 Unported Licence.

35 U. Rocha, K. U. Kumar, C. Jacinto, I. Villa, F. S. Rodríguez, M. d. l. C. I. d. l. Cruz, A. Juarranz, E. Carrasco, F. C. J. M. van Veggel, E. Bovero, J. G. Solé and D. Jaque, *Small*, 2014, **10**, 1141.
36 U. Rocha, C. Jacinto, W. F. Silva, I. Guedes, A. Benayas, L. M. Maestro, M. A. Elias, E. Bovero, F. C. J. M. van Veggel, J. G. Solé and D. Jaque, *ACS Nano*, 2013, **7**, 1188.
37 K. Binnemans, *Chem. Rev.*, 2009, **109**, 4283.
38 (*a*) A. S. Chauvin, F. Gumy, D. Imbert and J.-C. G. Bünzli, *Spectrosc. Lett.*, 2004, **37**, 517; (*b*) A. J. Steckl, M. Garter, D. S. Lee, J. Heikenfeld and R. Birkhahn, *Appl. Phys. Lett.*, 1999, **75**, 2184.
39 J. H. Kim and P. H. Holloway, *Adv. Mater.*, 2005, **17**, 91.
40 A. Bednarkiewicz, D. Wawrzynczyk, M. Nyk and W. Strek, *Opt. Mater.*, 2011, **33**, 1481.
41 K. Lunstroot, L. Baeten, P. Nockemann, J. Martens, P. Verlooy, X. Ye, C. G. Walrand, K. Binnemans and K. Driesen, *J. Phys. Chem. C*, 2009, **113**, 13532.
42 S. Moeller, A. Hoffmann, D. Knaut, J. Flottmann and T. Juestel, *J. Lumin.*, 2015, **158**, 365.
43 B. M. Brewer and M. Nicol, *J. Lumin.*, 1981, **23**, 269.
44 H. Dong, L.-D. Sun and C.-H. Yan, *Chem. Soc. Rev.*, 2015, **44**, 1608.
45 P. Samuel, T. Yanagitani, H. Yagi, H. Nakao, K. I. Ueda and S. M. Babu, *J. Alloys Compd.*, 2010, **507**, 475.
46 F. N. Sayed, V. Grover, S. V. Godbole and A. K. Tyagi, *RSC Adv.*, 2012, **2**, 1161.
47 Q. Xiao, Q. Zhou and M. Li, *J. Lumin.*, 2010, **130**, 1092.
48 J. L. Ferrari, K. de O. Lima, E. Pecoraro, R. A. S. Ferreira, L. D. Carlos and R. R. Goncalves, *J. Mater. Chem.*, 2012, **22**, 9901.
49 Pierre Villars, Material Phases Data System (MPDS), CH-6354 Vitznau, Switzerland; SpringerMaterials; sd_1622044 (Springer-Verlag GmbH, Heidelberg, 2014), http://materials.springer.com/isp/crystallographic/docs/sd_1622044; accessed: 13-06-2015.
50 M. Pedroni, F. Piccinelli, T. Passuello, S. Polizzi, J. Ueda, P. Haro-González, L. Martinez Maestro, D. Jaque, J. García-Solé, M. Bettinelli and A. Speghini, *Cryst. Growth Des.*, 2013, **13**, 4906.
51 (*a*) K. Lunstroot, P. Nockemann, K. Van Hecke, L. Van Meervelt, C. Görller-Walrand, K. Binnemans and K. Driesen, *Inorg. Chem.*, 2009, **48**, 3018; (*b*) H. F. Brito, O. L. Malta, M. C. F. C. Felinto, E. E. S. Teotonio, J. F. S. Menezes, C. F. B. Silva, C. S. Tomiyama and C. A. A. Carvalho, *J. Alloys Compd.*, 2002, **344**, 293.
52 L. Sun, Y. Qiu, T. Liu, H. Peng, W. Deng, Z. Wang and L. Shi, *RSC Adv.*, 2013, **3**, 26367.
53 R. L. Nigro, G. Malandrino, I. L. Fragala, M. Bettinelli and A. Speghini, *J. Mater. Chem.*, 2002, **12**, 2816.

This journal is © The Royal Society of Chemistry 2016